Influences of Composition on the Electrochemical Performance in Immiscible Sn−Al Thin Films as Anodes for Lithium Ion Batteries

Renzong Hu, Qian Shi, Hui Wang, Meiqin Zeng, and Min Zhu*

School of Materials Science and Engineering, South China University of Technology, Guangzhou 510640, People's Republic of China

Received: August 7, 2009; Revised Manuscript Received: September 8, 2009

Immiscible Sn−Al alloy films with various Sn contents were prepared by electron beam deposition to construct the matching of composition and electrochemical performance as anodes in lithium ion batteries. It was found that the Sn-rich film electrodes deliver relatively lower discharge capacities and present poor cycleability, whereas the Al-x wt % Sn ($40 \leq x \leq 60$) film electrodes show a good balance among cycling ability, fast Li$^+$ diffusion, and acceptable capacity of about 600 mA h g^{-1}. This is because they have unique microstructure features that were revealed by XRD, SEM, and TEM analysis. There are two types of Sn particles in the Al-40 wt % Sn alloy film, which are the faceted big Sn particles with a (100) [001] preferential orientation and the Sn nanocrystals homogenously dispered in the Al matrix. The influences of composition of electrodes on their cycle performance were discussed from the viewpoint of volume change and Li$^+$ diffusion kinetics in the film electrodes.

1. Introduction

To improve the performance of lithium ion batteries, great efforts have been made to design and develop advanced anode materials to replace the commercial carbonaceous materials. Among the varieties of alternative anode materials, the Sn-based alloys have been considered as one of the most promising alternatives and have been extensively researched.[1] So far, most of the studies were focused on the intermetallic compounds containing Sn and an element either inactive to Li$^+$, such as Cu$_6$Sn$_5$ and Ni$_3$Sn$_4$, or active to Li$^+$, such as Sn$_x$Sb and Sn$_x$Si.[2−8] As it is known, Al can also react reversibly with Li and deliver specific capacities of 993, 1490, and 2234 mA h g^{-1}, respectively, if LiAl, Li$_3$Al$_2$, and Li$_9$Al$_4$ phases form.[9] Therefore, the active/active composite consisting of Sn and Al has great potential as an anode material for its high specific capacity. However, the Sn−Al alloy system, which likewise agrees well with the concept of active/active composite, has been rarely envisioned to be used as anode materials in lithium ion battery before our reports.

Unlike the Sn−Sb and Sb−Al systems, Sn−Al is an immiscible alloy, in which there is no intermetallic phase but only two terminal solid solutions, being fcc (Al) and tetragonal (β-Sn) with a weak attractive interaction between them, as shown in the Sn−Al phase diagram.[10] This unique active/active composite would show different lithiation/delithiation mechanisms compared with those systems containing intermetallic compounds, such as Cu$_6$Sn$_5$, SnSb, etc., which involves the insertion and disproportionation. Moreover, based on the theoretical titration curves for reaction of lithium with metallic Sn and Al at ambient temperature,[1,11−14] it is known that the formation potentials of various Li−Sn phases are higher than those of Li−Al phases and this indicates that Sn and Al would sequentially react with Li. Accordingly, the buffer effect, which was proposed in systems such as the SnSb phase, may also be

realized in the Sn−Al system, and the cycleability of the anodes using the Sn−Al immiscible system would be enhanced.[4]

In our previous work, we reported preliminarily the electrochemical performance of the Sn−Al thin film electrodes for the first time.[15] It was found that the film electrodes with high Al content delivered a high initial discharge capacity, whereas the film electrodes with high Sn content showed a relatively better cycle performance. Meanwhile, there is a faster Li$^+$ transporting rate in the Sn-rich Sn−Al alloy film electrode compared with that of pure Al.[16] In the subsequent study, however, we have found that those Sn−Al thin film electrodes presented different structure and morphology due to their difference in composition and resulted in quite different electrochemical properties. Thus, a detailed and systematic investigation is required to clarify the correlation between microstructure and electrochemical properties and to optimize electrochemical performances of Sn−Al thin film electrodes. In the present work, the above subjects were investigated in detail by changing the composition systematically. On the basis of this research, the optimizing match of volume expansion and capacity was established in the Sn−Al system. The lithiation/delithiation mechanism of this alloy system was proposed, and the influence of factors (discharge nucleation potential, Li transport rate, current density) on their electrochemical performances were determined.

2. Experimental Section

2.1. Preparation of Sn−Al Alloy Film Anodes. The Sn−Al thin films were deposited on Cu foil substrates by an e-beam evaporator with two source units. In the deposition, a Sn layer was deposited on the Cu foil substrate first, and then a Sn−Al composite layer was covered on top, which was codeposited by evaporating Sn and Al target synchronously. The composition of the six thin films, as listed in Table 1, was controlled by adjusting the evaporation rate from each single source and finally measured by energy-dispersive X-ray spectroscopy (EDX). The thickness of the films was controlled to be nearly the same (about 2 μm) by the input power and evaporation time and

* To whom correspondence should be addressed. E-mail: memzhu@scut.edu.cn. Tel.: 86 20-87113924. Fax: 86 20-87111317.

18954 *J. Phys. Chem. C, Vol. 113, No. 43, 2009*

Hu et al.

TABLE 1: Summary of the Compositions of the Sn–Al Thin Films Prepared by Electron Beam Deposition

|	composition (wt %)		
sample	Al	Sn	named as
1	76	24	Al-24 wt % Sn
2	67	33	Al-33 wt % Sn
3	60	40	Al-40 wt % Sn
4	45	55	Al-55 wt % Sn
5	35	65	Al-65 wt % Sn
6	16	84	Al-84 wt % Sn

measured using the quartz crystal oscillation attached to the evaporator. The amount of the film was obtained by measuring the sample weight before and after film deposition with an FA1104N electronic balance.

2.2. Electrochemical Characterization. The electrochemical performance of the deposited film anodes was examined by using CR2016 coin-type half-cells assembled in an argon-filled glovebox. The cells were constructed using the as-deposited thin films as a working electrode and a lithium sheet as a counter/reference electrode with a polyethylene membrane as the separator. The electrolyte was $LiPF_6$ (1M) in mixture of EC + DEC + EMC (1:1:1 by volume). Galvanostatic charge–discharge measurements were carried out at room temperature using different current densities in various cutoff potential ranges for different purposes, which was controlled by an Arbin BT-2000 battery test system. Cyclic voltammograms (CVs) were measured by the AutoLab Electrochemical System (ECO Chemie) in the range of 0.0–2.0 V at scanning rates of 0.1, 0.2, 0.3, 0.4, 0.5, and 1 mV s^{-1}.

2.3. Materials Characterization. The microstructures of the thin film electrodes were characterized by X-ray diffraction (XRD) and scanning electron microscopy (SEM) using a Philips X'pert MPD with Cu Kα radiation and a LEO 1530 VP FE-SEM, respectively. The compositions of the samples were analyzed by an INCA300 EDS attached to the SEM. A JEM-2100 transmission electron microscope (TEM) operating at 200 kV was used to observe the microstructure of the as-deposited Al-40 wt % Sn thin films. The samples for TEM were thinned by a precision ion polishing system (gatan, model 691) from the Cu substrate side. The DSC measurement was performed for the as-deposited Sn–Al films using a Pyris Diamond DSC (PerkinElmer, USA) at a heating rate of 10 °C min^{-1}. For the electrochemically reacted samples, the sample holders of the XRD measurement were covered by polypropylene film to prevent reaction with moisture in the air.

3. Results

3.1. Microstructure of the As-Deposited Sn–Al Thin Film Electrode. Figure 1 shows the XRD patterns of the as-deposited Sn–Al thin films of different compositions. Besides those reflections from the Cu substrate and a small peak corresponding to reflection of the Cu_6Sn_5 intermetallic phase, which should be formed between the interface of the predeposited Sn layer and Cu foil substrate during the process of deposition, all other peaks for each Sn–Al thin film are attributed to the Al phase and the Sn phase. There is no evident shift of Al and Sn peaks, meaning that there is no obvious dissolving of Sn into Al or vice versa. However, as shown from diffractograms a–c in Figure 1, the Al-rich Sn–Al thin films, especially the Al-40 wt % Sn films, present a (100) [001] preferential orientation of Sn, whereas there is no obvious preferential orientation in the Sn-rich Sn–Al thin films, such as Al-84 wt % Sn shown in Figure 1, diffractogram f. There, the I_{101}/I_{200} (=23) of the Sn
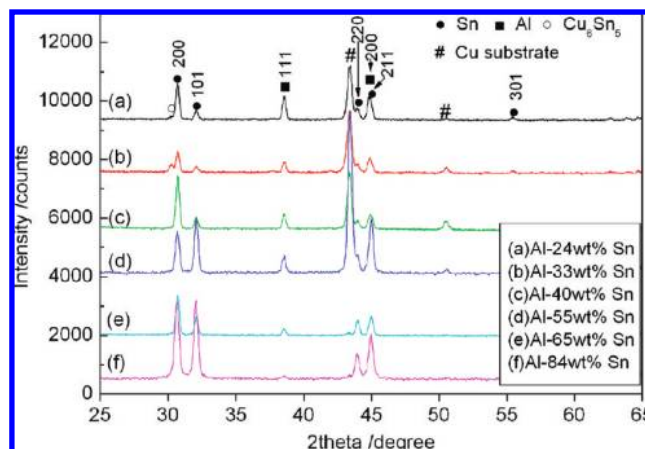
Figure 1. X-ray diffractograms of Al-*x* wt % Sn (*x* = 24, 33, 30, 55, 65, 84) thin films.
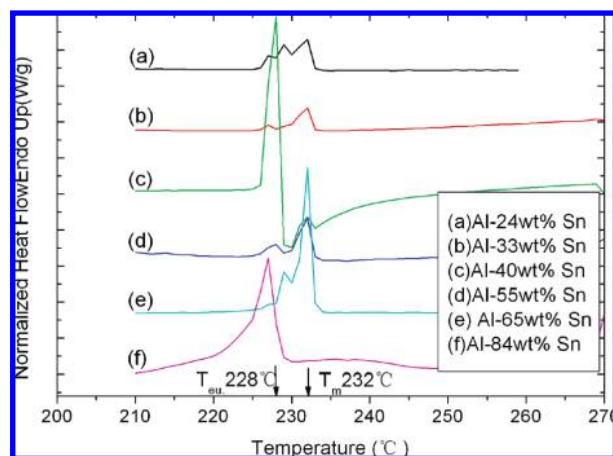
Figure 2. DSC curves of Al-*x* wt % Sn (*x* = 24, 33, 30, 55, 65, 84) thin films. The thin films were heated at the rate of 10 °C min^{-1} in nitrogen.

phase, being 0.9 in JCPDS no. 04-0673, in Figure 1, diffractogram c, is the highest, suggesting a high (100) [001] texture of Sn existed in the Al-40 wt % Sn alloy thin film. As will be discussed later, this resulted from that different solidification behaviors exist in the eutectic alloy thin films with different compositions and substantially affect their electrochemical performances.

DSC heating scanning curves for the six as-deposited Sn–Al alloy films are shown in Figure 2. T_m and $T_{eu.}$ given in Figure 2 are the standard melting point of Sn and eutectic point of Sn–Al, respectively. It can be seen that only one endothermic peak between 215 and 230 °C, which is believed to be caused by the reverse eutectic reaction of Sn–Al, is observed for the highly Sn-rich thin film, Al-84 wt % Sn (Figure 2, curve f). However, there are three endothermic peaks with onsets at 226.2, 227.5, and 230.1 °C, respectively, for the Al-rich Al-24 wt % Sn thin film (Figure 2, curve a). It suggests that different thermal changes exist in the Sn–Al thin films, which should be due to the differences in the microstructure induced by the composition change. The peak at 230.1 °C is attributed to the melting of Sn, whereas the former two peaks were supposed to be due to the reverse eutectic reactions that occur in two different kinds of Al–Sn boundary regions, big Sn particles with Al matrix and fine Sn particles with Al matrix, respectively, as indicated by the microstructures of Sn–Al thin films shown later. With respect to the Al-40 wt % Sn film, as shown in Figure 2, curve c, its thermal behaviors are quite different from those of the

Immiscible Sn−Al Thin Films

J. Phys. Chem. C, Vol. 113, No. 43, 2009 **18955**

others. There is a strong endothermic peak at 226.7 °C and a tiny endothermic peak at about 231.0 °C in the heating curve; the former peak is attributed to the eutectic reaction at interfaces of the Al and Sn phases, whereas the later peak is caused by the melting of the Sn phase in the film. This is because the reverse eutectic reaction takes place before melting of the Sn, according to the phase diagram of Al−Sn. However, both the eutectic and the melting temperatures in the Sn−Al alloy films is a bit lower than the theoretical ones, 228 and 232 °C, respectively, which is owing to the fact that Sn grains are very tiny and the nanosize effect causes the depression of the melting and eutectic point. The amount of heat release (ΔH) caused by Sn melting, obtained by integrating the area under the peak, is about 3.21 J g^{-1}. This value is much less than that caused by the reverse eutectic reaction of Al−Sn ($\Delta H = 42.75$ J g^{-1}), which shows that a large amount of Sn reacted with Al in the heating process of Al-40 wt % Sn film.

Figure 3 shows the SEM images of the as-deposited Al-24 wt % Sn, Al-40 wt % Sn, and Al-65 wt % Sn thin film surfaces. With respect to the Al-24 wt % Sn thin film, as shown in Figure 3a, the Al matrix (dark regions) continuously covering the substrate is composed of microsized particles, whereas most of the Sn particles (bright regions) with flower-like structures are randomly dispersed in it and the Sn particles on the surface penetrated through the boundaries and cavities of the Al matrix. The morphology of the Al-40 wt % Sn sample, shown in Figure 3b, is quite the same as that of the Al-24 wt % Sn sample, although its particle of the Al matrix is denser and larger, and the size of Sn particles is also larger than those of the Al-24 wt % Sn film. However, it should be emphasized that most of the Sn precipitates in this film have a faceted shape, as shown in an enlarged image in the inset in Figure 3b, indicating that the Sn particle growth proceeds via the development of energetically favorable surfaces. For the Sn-rich Sn−Al alloy, as Al-65 wt % Sn thin film shown in Figure 3c, the morphology and distribution of the Sn and Al phases are significantly different in comparison with the Al-rich Sn−Al films. There, the Sn grains were agglomerated and the microsized Al particles were dispersed on their surfaces. The above results reveal that the electron-beam-deposited Sn−Al thin film electrodes presented different microstructure and morphology due to the difference in composition.

TEM analysis was performed to further investigate the microstructure of the Sn−Al thin films. Figure 4 shows the typical plan-view images of the Al-40 wt % Sn thin film. As shown in Figure 4a, the big, faceted Sn particles (dark regions) are embedded in the Al matrix (bright regions) and appear to be well-separated. According to their SAED patterns, as shown in the inset of Figure 4a, all of the big Sn particles are single crystals, indicating that only one nucleation event takes place in each Sn liquid zone, and then the postnucleation growth rate is very fast. Moreover, the faceted shape of the Sn particles indicates that their growth proceeds via the development of energetically favorable surfaces, which most likely is attributed to the highly anisotropic tetragonal crystal structure of Sn. With respect to the Al matrix, as shown in Figure 4b, it is polycrystalline with a grain size of about 0.5 μm. The inset shown in Figure 4b is the SAED pattern for one of the Al crystals. It is interesting to note that many small particles with a size of about 10 nm, as shown in Figure 4c, are homogeneously dispersed in the Al matrix. As confirmed by the SAED pattern shown in the inset in Figure 4c, those nanoparticles are Sn. These observations reveal that the Sn phase has two characteristic distributions in the Al matrix. One is the faceted,
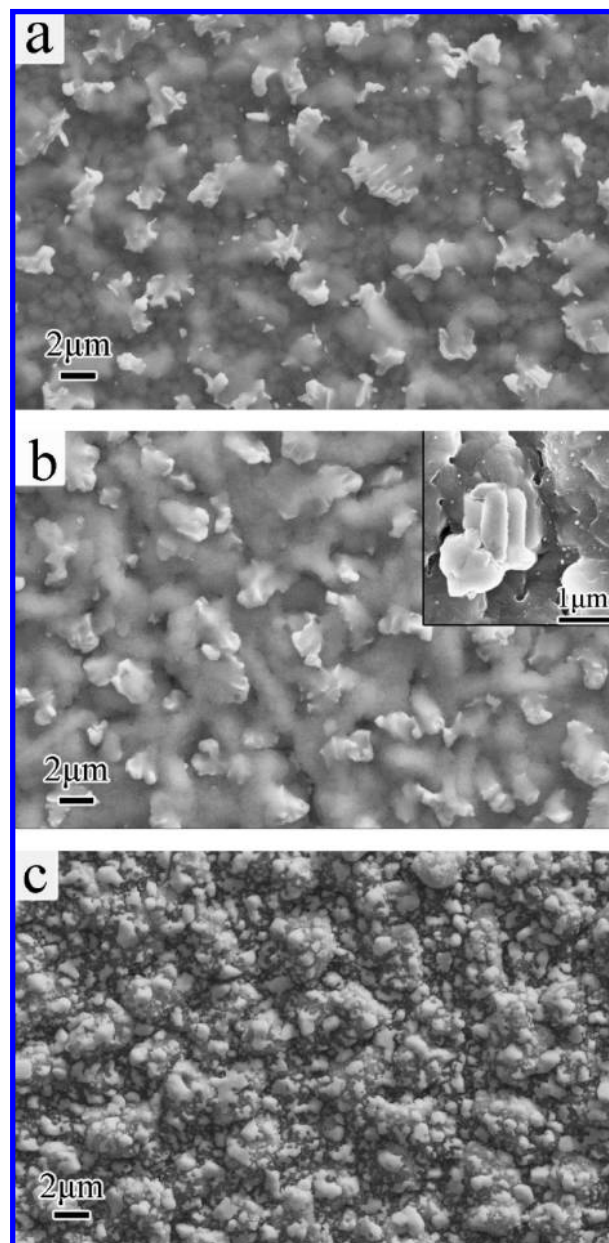
Figure 3. SEM images of (a) Al-24 wt % Sn, (b) Al-24 wt % Sn, and (c) Al-65 wt % Sn thin films. Back-scattering images: bright regions represent Sn, and dark regions represent Al.

big particles, which are nucleated and formed during the final eutectic reaction, and the other is the nanocrystals, which are supposed to be precipitated from the supersaturated solid solution of α(Al) when the thin film is slowly cooling to room temperature. The two kinds of distribution of the Sn phases in the Al matrix are quite dependent on the composition (Al, Sn) of the thin films in which different DSC thermal behaviors were presented, as shown in Figure 2. With respect to the Al-40 wt % Sn thin film, the endothermic peak appeared at the eutectic temperature on the DSC curve shown in Figure 2, curve d, which is the highest in comparing with the others, and is attributed to that the Sn−Al eutectic reaction occurs accompanying with the nano Sn particles melting due to the nanosize effect causes the depression of the melting point. It is worthy of note that, more importantly, the different crystallinity and distribution of Sn−Al alloy films will induce quite different electrochemical performances as anodes in lithium ion batteries.
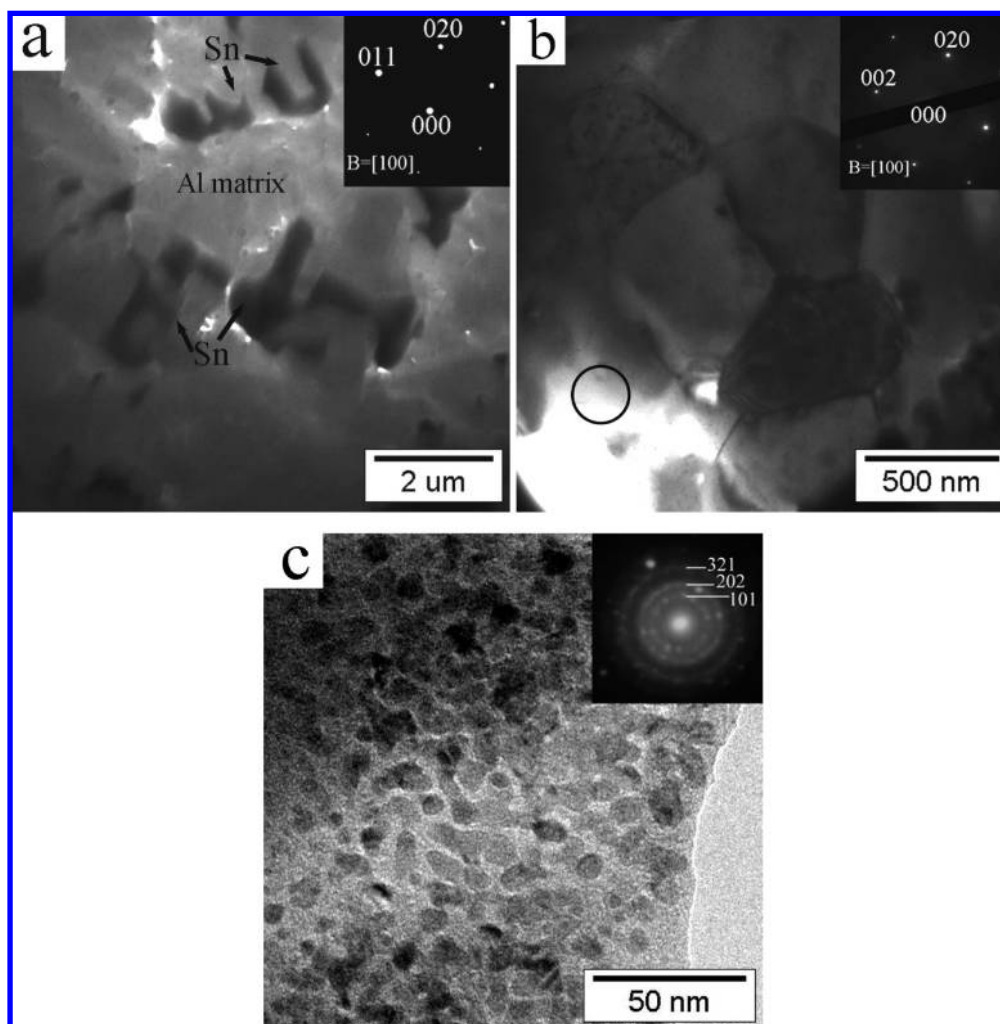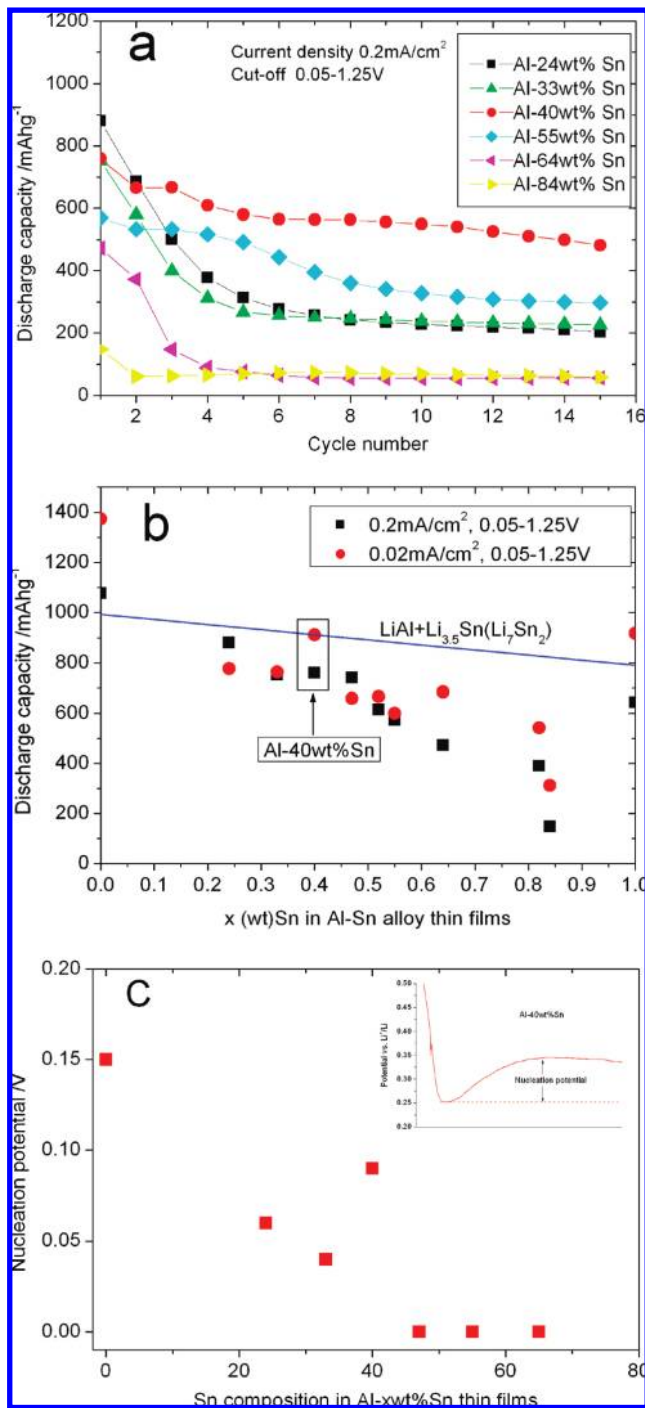
Figure 4. (a) Low-magnification TEM image of the Al-40 wt % Sn thin film and the selected area diffraction (SAED) pattern (inset) of Sn particles, (b) TEM image and SAED pattern (inset) of the Al matrix, and (c) high-magnification TEM image of an area circled in (b) and the SAD pattern (inset) for the fine dark regions (Sn nanocrystals).

3.2. Cycling Ability, Discharge Capacity, and Nucleation Potential of the Sn−Al Alloy Film Electrodes. Figure 5 compares the cycling performance of all the six thin film electrodes cycled between 0.05 and 1.25 V under a current density of 0.2 mA cm^{-2}. Although similar multiplateau characteristics are presented on the charge/discharge curves of these electrodes, it is observed in Figure 5a that the Sn-rich thin film electrodes (Al-65 wt % Sn and Al-84 wt % Sn) deliver relatively lower discharge capacities and present poor cycleability, whereas the Al-rich thin film electrodes (Al-24 wt % Sn and Al-33 wt % Sn) can yield high initial discharge capacities of about 800 mA h g^{-1}, but unfortunately 70% of these capacities are lost after several cycles. It is interesting to note, however, that the Al-x wt % Sn (40 ≤ x ≤ 60) film electrodes show a good balance between improved cycling ability and acceptable capacity, indicated by that the Al-40 wt % Sn and Al-55 wt % Sn electrodes can yield a reversible capacity of about 600 and 400 mA h g^{-1}, respectively. In particular, as shown in Figure 5a, the electrode with a composition of Al-40 wt % Sn has the highest capacity and the best cycleability in comparison with the thin film electrodes of other different compositions. It is believed to be attributed to its unique crystallinity and distributions of the Sn phase and the Al matrix, as shown in Figure 4, which is supposed to be favorable to improving the Li transport kinetics and keeping the thin film structure stable, and it will be discussed in a later section.

Figure 5b summarizes the initial discharge capacities of these Sn−Al thin film electrodes cycled under a low current density of 0.02 mA cm^{-2} and a high current density of 0.2 mA cm^{-2}. It clearly shows that the initial discharge capacity decreased with increasing of the Sn component under both current densities, which is consistent with the theoretical calculation results (the solid line) as well as our previous results that the Al element is a main reactant in the initial cycling of these thin film Sn−Al electrodes.[16]
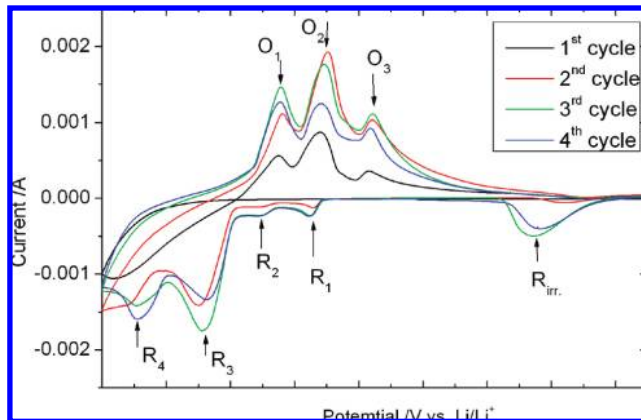
The energy barrier for the nucleation of the LiAl phase from Al and/or Al(Li) solid solution in the initial cycles, defined as the discharge nucleation potential, could be measured from the small dip in the discharge curve, as illustrated in the inset in Figure 5c.[17] Figure 5c shows that the discharge nucleation potential of the first cycle decreases as the Sn content increases. This trend can be explained by the reduction of the Al grain size and the increase of the interface region (mainly the Al−Sn boundaries) in the thin film as the Sn content increases, as well as possibly the existence of the more active Sn phase within the film.[18] However, the discharge nucleation potential of the Al-40 wt % Sn electrode is much higher than that of any other sample tested, which may be due to the high (100)[001] texture in this film. The presence of the preferential orientation apparently minimizes energy at the film top surface and substrate interface. Thus, extra energy is required for Li to transport into the active material layer in the film. The above results indicate
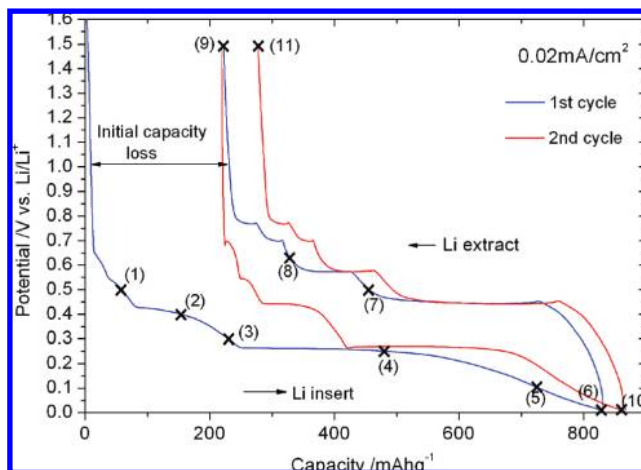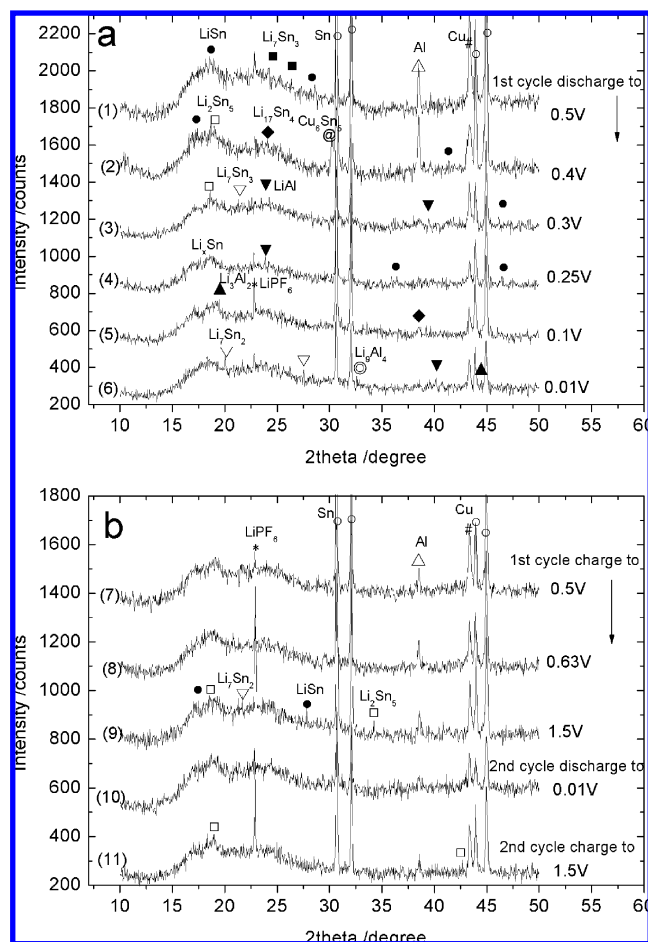
Figure 6. Cyclic voltammograms (0.5 mV s^{-1}) for the Al-40 wt % Sn thin film electrode.

Figure 7. Charge−discharge curves of the initial two cycles for the Al-40 wt % Sn thin film electrode under a current density of 0.02 mA cm^{-2}.

whereas three oxidation peaks appear at 0.55 V (O$_1$), 0.70 V (O$_2$), and 0.84 V (O$_3$) for charging. This reveals the process of reversible reaction between the Sn−Al alloy and Li and the electrochemical activities of the immiscible Sn−Al alloy film. However, in the first scanning cycle, there is only a broad reduction peak below 0.10 V, indicating Al as the dominant reactant in the first discharge cycle, which can be confirmed by the cyclic voltammogram of metallic Al.[16] It is noticeable that an irreversible reduction peak (R$_{irr.}$) appears at 1.5−1.3 V versus Li/Li$^+$ since from the second reduction half-cycle. This current peak, at which the potentials are much higher than those for Li alloy phase formation, may be caused by the irreversible side reactions of electrolyte decomposition and leads to SEI formation.[19] This side reaction became severe after an active step in the first Li insertion/extraction cycle because more surfaces would contact with the electrolyte as cracks was formed in the film. This resulted in an increase of the irreversible capacity loss. On the basis of this result, a suitable cutoff potential range for this Sn−Al electrode should be chosen to avoid the irreversible side reaction, which should be below 1.3 V for the upper (charge) limit.

Figure 7 shows the voltage versus capacity curve of the initial two discharge/charge cycles of a Li/Al-40 wt % Sn cell cycled under a current density of 0.02 mA cm^{-2} between 1.5 and 0.01 V. It is evident that several processes take place during the discharge and charge reactions that are associated with various lithium alloying and dealloying stages. Furthermore, quite

Figure 5. (a) Cyclic performances of Sn−Al thin film electrodes tested between 0.05 and 1.25 V under a current density of 0.2 mA cm^{-2}. (b) The dependence of initial discharge capacity on the composition of Sn−Al thin film electrodes. The calculated specific capacity of the Sn−Al alloy in the case of LiAl + Li$_{3.5}$Sn is also shown. (c) The dependence of the initial discharge nucleation potential on Sn composition of Sn−Al thin film electrodes.

that the composition and the microstructure of these Sn−Al thin film electrodes have great influence on their capacities and cycle performances.

3.3. Lithiation/Delithiation Mechanism of Al-40 wt % Sn Film Electrode. Figure 6 shows the cyclic voltammograms of the Al-40 wt % Sn thin film electrode. For the Al-40 wt % Sn film electrode, well-resolved reduction peaks appear at about 0.65 V (R$_1$), 0.50 V (R$_2$), 0.32 V (R$_3$), and 0.11 V (R$_4$) for discharging during the second cycle and the subsequent cycles,

Figure 8. Ex situ XRD patterns of the Al-40 wt % Sn thin film electrode at various discharge/charge steps. The selected steps are shown in Figure 9.

Figure 9. XRD patterns of the Al-40 wt % Sn thin film electrodes after long-time discharging to 0.01 V in the first cycle at a low current density of 0.01 mA cm⁻².

similar plateau characterizations in the first and the second and the subsequent cycles suggests the well reversibility of lithiation/delithiation reactions in these Al-40 wt % Sn thin films. The multiplateau behavior of this immiscible alloy electrode, where the distinct plateaus are at about 0.65, 0.55, 0.44, and 0.25 V in the second discharge curve, is attributed to the successive electrochemical reactions of the Sn phase and Al phase, which is consistent with the results of CVs, as shown in Figure 6.

To determine the reaction mechanism and structure change of the thin film electrode in Li insertion−extraction processes, XRD analysis, shown in Figure 8, was carried out at different depths of discharge and charge, as labeled in Figure 7. It was found that the surface morphology of the thin films became rougher significantly after electrochemical reaction in the batteries, which was supposed to be responsible for the relatively high background in the diffraction patterns. However, by careful inspection of the XRD results, the phase formation and structure change in the thin films during discharging/charging can be detected. As shown in Figure 8a (pattern 1), in addition to the appearance of some reflection peaks belonging to LiSn and Li_7Sn_3, the preferential (100)[001] orientation of Sn disappeared after the initial lithium insertion process down to 0.5 V (depth point (1) in Figure 7), indicating rearrangement of the film structure and reaction of part of the Sn phase. The peak attributed to (111) of Al is still obvious. However, as shown in Figure 8a (pattern 4), while the thin film electrode was discharged to 0.25 V (depth point (4) in Figure 7), the diffraction peaks of Al disappeared and the LiAl phase was formed. This
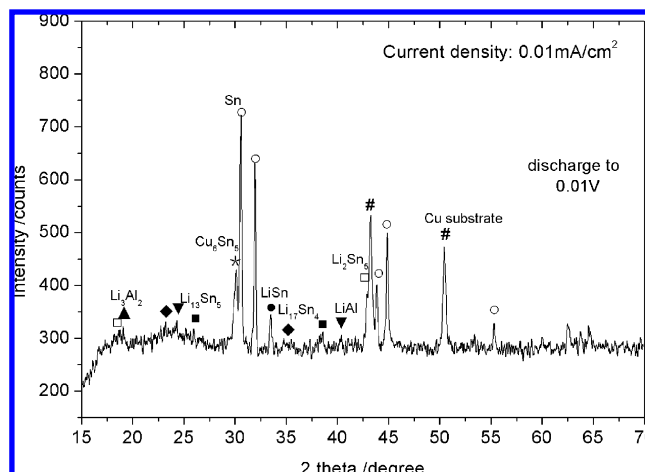
suggested that the long discharge plateau at 0.25 V, as shown in Figure 7, was attributed to the formation of the Li−Al alloy phase. The Li-rich Li−Sn and Li−Al phases (Li_7Sn_2, Li_3Al_2, etc.) were formed after the Sn−Al thin film electrode was deeply discharged to 0.01 V. When the Li was extracted during charging to 0.5 V (point (7) in Figure 7), as shown in Figure 8b (pattern 7), the reflection peaks of the Al phase could be observed again, indicating that decomposition of Li−Al alloy phases and recrystallization of Al occur in the 0.45 V plateau on charge curves. This is different from the pure Al thin film electrode, in which the recrystallization of Al was not observed even to the end of charge. However, some Li−Sn phases were not decomposed and remained; even the electrode was deeply charged to 1.5 V, as shown in Figure 8b (pattern 9). When the electrode discharged again to a potential of 0.01 V in the second cycle (point (10) in Figure 7), the reflections of Sn were obviously weakened and those of Al disappeared again, suggesting that both Sn and Al phases were active with lithium, although no definite diffraction peaks of Li−Sn and Li−Al phases but rather two wide random scattering peaks could be identified between 15° and 25°. This suggests a possibility that the Sn−Al alloy film reacts with Li and results in a formation of nanocrystalline or amorphous in some regions of the film when the cycles were prolonged. However, the existence of Sn peaks in the diffractograms (6, 10) in Figure 8 indicated that some Sn in the film, possibly that in the inner layer, was inactive with lithium and remained. This is possibly the main reason for the difference between actual discharge capacities of 831 mA h g⁻¹ and the theoretical capacity of 993.4 mA h g⁻¹ given by [0.60 × 993₍LiAl₎ + 0.40 × 994₍Li4.4Sn₎]. This speculation was confirmed by the further XRD result, shown in Figure 9, for the thin film electrode reacted with lithium at a low current density of 0.01 mA cm⁻² for longer time (discharging about 51 h). It shows that quite an amount of Sn phase did not react with lithium and retained. These results suggest that the microstructure of thin film should be further optimized to quicken electrolyte immerging and Li⁺ transport. Moreover, it is clear that a peak at 30.0 °C in Figure 9, as well as in Figure 8a (pattern 2), which was attributed to the Cu_6Sn_5 phase, appeared when the electrode discharged. This indicates that there was a mutual diffusion in the interface between the Sn and the Cu substrate under the action of current in the electrode. It may influence the electrochemical performance of these Sn−Al thin film electrodes. However, this issue is not included in the scope of the present work and will not be further considered here.

Immiscible Sn−Al Thin Films

J. Phys. Chem. C, Vol. 113, No. 43, 2009 **18959**

4. Discussion

4.1. Structural Formation in the Sn−Al Thin Films. The above-mentioned microstructure features in those Sn−Al films with various compositions can be understood from their solidification and film growth. As is well-known, the Sn−Al is a simple binary eutectic alloy system undergoing a eutectic transformation at 228 °C (97.6 wt % Sn, 2.4 wt % Al). A very important feature of this class of materials is the thermodynamic immiscibility of the constituents (Al and Sn) and their highly different mobilities in the growth zones during deposition. For Sn−Al films deposition, due to low melting point of Sn (232°), the evaporation and deposition rate of Sn was high. Therefore, coarse polycrystal grains of Sn were formed in the predeposited Sn layer. However, the Sn underlayer would be melted while covered by the codeposited Al−Sn films because extra heat was brought to the film when the Al particles were deposited as the fact that the melting point of Al (660.5°) is much higher than that of Sn. Thus, the thin films were grown accompanying a solidification process of the Al−Sn liquid. With respect to the Al-rich Sn−Al thin film, during cooling and the film growth, most of the Al (75.9% Al in the case of Al-24 wt % Sn) first solidified from the liquid before reaching the eutectic temperature to form a big continued solid (see Figure 3a). Because this solidification process is very rapid in the film deposition, some Sn cannot separate out to reach equilibrium and remains in Al to form a supersaturated solid solution, which will finally precipitate to form tiny Sn particles and disperse in the Al matrix while the thin film is slow cooling to room temperature. However, for the Sn-rich Sn−Al alloy thin film, the amount of the proeutectic alpha phase (Al) is small and cannot form a continued matrix while the amount of the eutectic beta (Sn) is large and finally solidifies to form big agglomerations, as shown in Figure 3c. Considering the above results in Figures 1−3, it is suggested that the Sn−Al alloy film with middle Sn content, especially the Al-40 wt % Sn thin film, experiences a quite different solidification behavior during film growth.

According to the phase diagram, when the temperature is higher than the eutectic temperature, about 60% of the Al in the Al-40 wt % Sn thin film, less than that of the Al-rich Sn−Al film, such as the Al-24 wt % Sn, will first solidify from the Sn−Al liquid to form a big continued solid Al matrix with quite an amount of the Sn supersaturated in it due to the nonequilibrium solidification process in the film deposition and then precipitated and dispersed in the primary alpha (Al) phase later, while most of the remained Al−Sn liquid stayed in the narrow gaps and boundaries between the primary Al grains. There is a high surface tension, that is, high interface energy, between the liquid Sn phase and the primary alpha (Al) phase due to that the Sn and Al phases are immiscible. Thus, the remained Sn liquid is inclined to form a spherical shape to reduce its surface energy. However, most of the Sn phases present a lamellar, facet shape in films, as shown in SEM images (see Figure 3a,b) and the TEM results (see later), due to that the shape transformation is depressed by the shape of the gaps and the grain boundaries of the primary Al matrix. As the thin film is cooling to the eutectic temperature, the melted Sn in the gaps and grain boundaries will be apt to move to the near surface of the thin films (see Figure 3) by the combined effects of gravitation and surface tension and the compressive stress, accompanying the remaining Al−Sn liquid solidifying at a very fast rate to reduce the Al/Sn interface energy.[20] However, it is well-known that the {100}$_{Sn}$ facets have the highest interfacial energy and thus there is the fastest growth rate in the [100] direction. Accordingly, it produces a [100] preferential orientation for the Sn
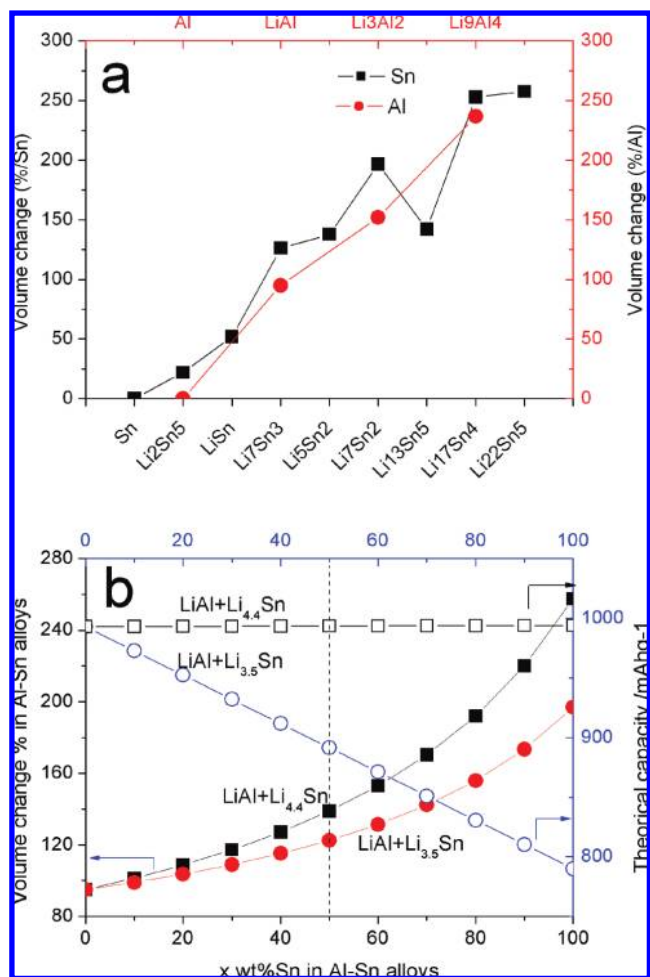
Figure 10. Dependence of volume change ($\Delta V\%$) on Sn composition for transformations of Sn → Li_xSn_y and Al → Li_xAl_y (a) and volume change ($\Delta V\%$) of lithiated Al-x wt % Sn alloys with two models of LiAl + $Li_{4.4}$Sn and LiAl + $Li_{3.5}$Sn were considered (b). The theoretical capacity of Al-x wt % Sn (mAh/g) as a function of Sn composition (x) in both cases is also shown. *The volume of each phase was calculated based on the structure data given in the JCPDS database.

phase while the remaining liquid Sn crystallized with relaxing the most heat (ΔH) comparing with those in other directions. As shown in Figure 1, diffractogram c, the Al-40 wt % Sn thin film has the most remarkable [100] texture comparing other films considered here, indicating that the most liquid Sn is remained in the gaps and grain boundaries of the Al matrix and finally solidified and crystallized in the [100] direction during the eutectic reaction, while the most heat is relaxed in this film, as confirmed by the DSC result in Figure 2, curve c.

4.2. Designation of the Alloy Composition. Figure 10a shows that the Sn and Al would suffer a large volume change when they form various Li_xSn and Li_yAl phases during their lithiation process. The volume expansion is 258, 197, and 95% when $Li_{22}Sn_5$, Li_7Sn_2, and LiAl are formed, respectively, whereas it is only 9% for lithiated graphite.[17] In this immiscible system, however, the Sn and Al exist as primary phase with a weak interaction between them, and thus, the total volume expansion in the Sn−Al alloys should be the superposition of the volume expansion in the two transformations, Sn → Li_xSn and Al → Li_yAl. Figure 10b shows the calculated volume expansion ($\Delta V\%$) of the Al-x wt % Sn alloy as a function of composition (x wt % Sn) by taking LiAl + $Li_{4.4}$Sn and LiAl + $Li_{3.5}$Sn as the combinations of lithiated phases. Capacity was also presented as a function of the composition (x wt % Sn) in
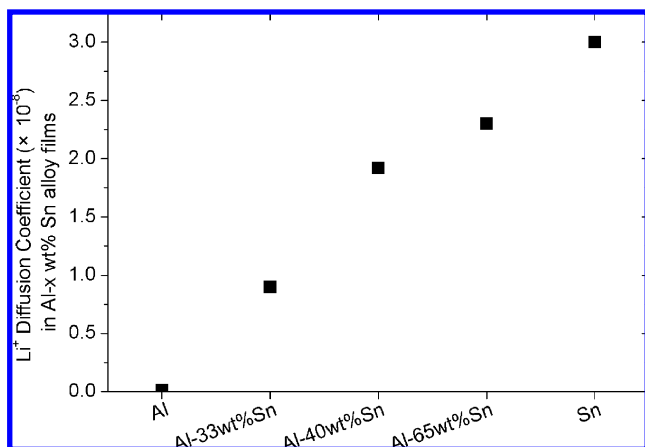
Figure 11. Li^+ diffusion coefficient (D_{Li+}, cm^2 s^{-1}) in Sn–Al thin film electrodes.

Figure 10b in both cases of LiAl + Li$_{4.4}$Sn and LiAl + Li$_{3.5}$Sn. It is obvious from Figure 10b that the $\Delta V\%$ increases with the increase of Sn over the range of 0–100 wt % Sn and the volume change in the case of the LiAl + Li$_{4.4}$ Sn model is larger than that of the LiAl + Li$_{3.5}$ Sn. However, a rapid increase in volume expansion occurs when the Sn content is over about 60 wt % Sn in both cases of LiAl + Li$_{4.4}$Sn and LiAl + Li$_{3.5}$Sn, suggesting that the Sn-rich Sn–Al alloy electrodes would suffer larger volume expansion, leading to poor cycle performance in the electrodes. With respect to the capacity, on the other hand, the capacity of the Al-x wt % Sn alloy electrodes was decreased with increasing the Sn component (x wt %) for the cases of both LiAl + Li$_{3.5}$Sn and LiAl + Li$_{4.4}$ Sn. Accordingly, we suppose that the Al-rich Al-x wt % Sn alloy electrodes ($x < 50$) would have better performances, combining relatively good cycleability with high capacity. However, as mention above, the pure Al thin film has very slow Li$^+$ diffusion, which is apt to generate potential polarization on the electrode, and thus, lower capacity can only be obtained in the practical electrodes especially when current density was high.

The lithium diffusion coefficient in this Al-40 wt % Sn thin film electrode was estimated according to a method previously reported.[16] The diffusion coefficient of Li$^+$ in the Al-40 wt % Sn thin film electrode was determined to be 1.92×10^{-8} cm^2 s^{-1} at 298 K. This value is a bit lower than the Li$^+$ diffusion coefficient in the Li–Sn alloy phases but nearly 4 orders of magnitude higher than that of Li$^+$ diffusion in the pure Al thin film.[9,12] This should be attributed to the unique structure and morphology of the e-beam-deposited Sn–Al films.

Figure 11 summaries the Li$^+$ diffusion coefficient in some of the Sn–Al alloy thin film electrodes we previously tested. It can be seen that the Li$^+$ diffusion coefficient increases as the Sn content in Sn–Al thin film electrodes increases, suggesting that the lithium transport kinetics in Al-based electrodes can be much enhanced by well dispersing a suitable amount of Sn phase in the Al matrix. On the basis of the above consideration, the reasons for the alloy thin film electrode with a composition of Al-40 wt % Sn having the best cycle performance, as shown in Figure 5, are summarized in the following:

(a) The suitable Al/Sn ratio makes the thin film electrode keep high structure stability during Li insertion and extraction. The calculated volume change in the fully lithiated Al-40 wt % Sn thin film is about 120%, which is almost 2 times lower than that of the pure Sn electrode. Moreover, the Sn phase has relatively low elastic modules and two types of morphology, fine single-crystalline particles and the faceted big particles, fully

embedded and dispersed in the Al matrix, and can absorb large stress and strain during cycling and thus reduce the pulverization of active materials in electrode.

(b) The unique crystallinity and distribution of Sn and Al phases in the Al-40 wt % Sn thin film is favorable to enhance Li diffusion in Al matrix and yield the higher capacity. The fine Sn particles (about 10 nm in size) as well as the Sn–Al interface and the grain boundary serve as the transport channel for Li$^+$ in the Al matrix and improve its diffusion kinetics to ensure more materials be active to Li during discharging. Furthermore, the fast Li$^+$ diffusion can also reduce the potential polarization and, thereby, the electrode discharge and charge in long time to deliver more capacity.

5. Conclusions

In the present work, we investigated in detail the microstructure, electrochemical performance, and their correlation of the Sn–Al film electrodes by changing the composition systematically. On the basis of this research, the optimizing match of volume expansion and capacity as anode for lithium ion batteries has been established in the immiscible Sn–Al alloy system. The Sn–Al thin films with different compositions have quite different microstructure features and induce different properties on thermodynamics and anode behaviors. The initial discharge capacity and the nucleation potential decrease with increasing the Sn content in the Sn–Al alloy electrodes. The Sn-rich thin film electrodes deliver relatively lower discharge capacities, whereas the Al-rich thin film electrodes yield high initial discharge capacities but have poor cycleability. The Al-40 wt % Sn alloy film, in which faceted Sn particles with a (100) [001] preferential orientation and Sn nanocrystals homogenously disperse in the Al matrix, has the best performances, combining relatively good cycleability and a high capacity of about 600 mA h g^{-1} with fast Li$^+$ diffusion as anode materials for lithium ion batteries. Cyclic voltammograms and ex situ XRD results confirmed that Sn was more active than Al element and reacts first in the Sn–Al electrodes.

References and Notes

(1) Winter, M.; Besenhard, J. O. *Electrochim. Acta* **1999**, *45*, 31.
(2) Larcher, D.; Beaulieu, L. Y.; Macneil, D. D.; Dahn, J. R. *J. Electrochem. Soc.* **2000**, *147*, 1658.
(3) Hassoun, J.; Panero, J. S.; Simon, P.; Taberna, P. L.; Scrosati, B. *Adv. Mater.* **2007**, *19*, 1632.
(4) Yang, J.; Takeda, Y.; Imanishi, N.; Yamamoto, O. *J. Electrochem. Soc.* **1999**, *146*, 4009.
(5) Wachtler, M.; Winter, M.; Besenhard, J. O. *J. Power Sources* **2002**, *105*, 151.
(6) Beaulieu, L. Y.; Eberman, K. W.; Krause, L. J.; Dahn, J. R. *Electrochem. Solid State Lett.* **2001**, *4*, A137.
(7) Hatchard, T. D.; Topple, J. M.; Fleishauer, M. D.; Dahn, J. R. *Electrochem. Solid State Lett.* **2003**, *6*, A129.
(8) Beaulieu, L. Y.; Hewitt, K. C.; Dahn, J. R. *J. Electrochem. Soc.* **2003**, *150*, A419.
(9) Hamon, Y.; Brousse, T.; Jousse, F.; Topart, P.; Buvat, P.; Schleich, D. M. *J. Power Sources* **2001**, *97–98*, 185.
(10) Massalski, T. B., Ed. *Binary Alloy Phase Diagram [M/CD]*, 2nd ed.; ASM International: Materials Park, OH, 1996.
(11) Yin, F.; Su, X.; Li, Z.; Wang, J. *J. Alloys Compd.* **2005**, *393*, 105.
(12) Huggins, R. A. *Solid State Ionics* **1998**, *113–115*, 57.
(13) Hirai, K.; Ichitsubo, T.; Uda, T.; Miyazaki, A.; Yagi, S.; Matsubara, E. *Acta Mater.* **2008**, *56*, 1539.

(14) Courtney, I. A.; Tse, J. S.; Mao, O.; Hafner, J.; Dahn, J. R. *Phys. Rev. B* **1998**, *58*, 15583.

(15) Hu, R. Z.; Zhang, L.; Liu, X.; Zeng, M. Q.; Zhu, M. *Electrochem. Commun.* **2008**, *10*, 1109.

(16) Hu, R. Z.; Zeng, M. Q.; Li, C. Y. V.; Zhu, M. *J. Power Sources* **2009**, *188*, 268.

(17) Wang, C. Y.; Meng, Y. S.; Ceder, G.; Li, Y. *J. Electrochem. Soc.* **2008**, *186*, A615.

(18) Wang, J. C.; Appleby, A. J.; Little, F. E. *J. Power Sources* **2001**, *93*, 174.

(19) Winter, M.; Appel, W. K.; Evers, B.; Hodal, T.; Möller, K. C.; Schneider, I.; Wachtler, M.; Wagner, M. R.; Wrodning, G. H.; Besenhard, J. O. *Monatsh. Chem.* **2001**, *132*, 473.

(20) Lee, B. Z.; Lee., D. N. *Acta Mater.* **1998**, *46*, 3701.